

A continuum treatment of sliding in Eulerian simulations of solid-solid and solid-fluid interfaces

By A. Subramaniam, N. S. Ghaisas AND S. K. Lele

1. Motivation and objectives

Many engineering applications involve large elastic-plastic deformations in solids that may be coupled with fluid flows. In particular, Inertial Confinement Fusion (ICF), cavitation erosion, and impact welding involve shock waves, rapid deformation and plasticity with significant material deformation. Numerical simulations of such phenomena typically use either a Lagrangian or an Arbitrary Lagrangian-Eulerian (ALE) framework. Lagrangian methods perform poorly in large deformation conditions due to highly anisotropic meshes, entanglement and severe time step restrictions. ALE methods circumvent these problems by periodically remapping the field variables to an Eulerian grid which introduces additional numerical dissipation. Due to these disadvantages of Lagrangian and ALE methods, Eulerian methods are better suited for problems involving large material deformations. They are also ideally suited for simulating wave propagation and flow-like phenomena. The governing equations for tracking non-linear elastic deformations in a solid in a fully Eulerian frame were introduced by Godunov & Romenskii (1972) and by Plohr & Sharp (1989). Plohr & Sharp (1992) extended the equations to account for plasticity. These formulations used the deformation gradient tensor to track material deformations. An alternate, equivalent formulation based on the inverse of the deformation gradient tensor was presented by Trangenstein & Colella (1991).

In Eulerian methods, imposing internal boundary conditions such as material interfaces requires additional numerical treatment. One common approach is to use a level set to track the interface location and use appropriate jump conditions at the interface (López Ortega *et al.* 2014). Another approach is to treat the interface as numerically diffuse and solve for mixture fields that asymptotically approach the sharp interface limit (Ndanou *et al.* 2015; Subramaniam *et al.* 2017). The advantage of a diffuse interface approach over a level-set approach is that it is discretely mass conserving while level set methods are not and leak mass over time. When materials on either side of a material interface are not molecularly bonded, treating sliding at the interface is important. Such an interface should allow the materials to slide with respect to each other. In Eulerian simulations that use level-set methods, sliding at an interface can be accounted for by changing the Riemann solver at the interface to allow for slip (López Ortega *et al.* 2014). In a diffuse interface continuum numerical model for such an interface, treating sliding and allowing for a relative slip is not as straightforward. Favrie & Gavrilyuk (2012) treat sliding by performing a first-order extrapolation of the interface tangential velocity and then directly setting the tangential stress to zero. Additionally, their method is based on a one-dimensional setting and is not easily generalizable to multiple dimensions. The objective of this work is to develop a general algorithm that allows for sliding behavior at a material interface which can be applied to any Eulerian, diffuse interface numerical model.

The governing equations and numerical procedure for elastic-plastic deformations in

a multi-material context are presented in Section 2. The Eulerian sliding algorithm is described in Section 3. Results from one- and two-dimensional test cases are presented in Sections 4.1 and 4.2. The Richmyer-Meshkov instability between copper and aluminum with a sliding interface is presented in Section 4.3 and contrasted with the case where the materials are molecularly bonded at the interface before the conclusions in Section 5.

2. Governing equations

The governing equations describing non-linear elastic and plastic deformations of multiple solids and/or fluids are briefly described in this section. For a more detailed description of the governing equations and numerical methodology, we refer the reader to Ghaisas *et al.* (2016) and Subramaniam *et al.* (2017).

The fundamental equations governing the motion of a multi-material continuum in Eulerian form are the mass, momentum and energy equations shown here in index notation

$$\frac{\partial \rho Y_m}{\partial t} + \frac{\partial \rho Y_m u_k}{\partial x_k} = -\frac{\partial (J_m^*)_i}{\partial x_i}, \quad (2.1)$$

$$\frac{\partial \rho u_i}{\partial t} + \frac{\partial}{\partial x_k} [\rho u_i u_k - \sigma_{ik}] = \frac{\partial \tau_{ik}^*}{\partial x_k}, \quad (2.2)$$

$$\frac{\partial}{\partial t} \left[\rho \left(\varepsilon + \frac{1}{2} u_j u_j \right) \right] + \frac{\partial}{\partial x_k} \left[\rho u_k \left(\varepsilon + \frac{1}{2} u_j u_j \right) - \sigma_{ik} u_i \right] = \frac{\partial}{\partial x_k} [\tau_{ik}^* u_i - q_k^*]. \quad (2.3)$$

\mathbf{u} is the velocity and Y_m is the mass fraction of material m . ρ , ε and $\underline{\sigma}$ are the mixture density, internal energy and Cauchy stress, respectively, given in terms of species-specific quantities ρ_m , ε_m and $\underline{\sigma}_m$ by $\rho = \sum_{m=1}^M \alpha_m \rho_m$, $\varepsilon = \sum_{m=1}^M Y_m \varepsilon_m$ and $\underline{\sigma} = \sum_{m=1}^M \alpha_m \underline{\sigma}_m$, where α_m is the volume fraction of material m and M is the total number of materials. The volume fractions have to satisfy the constraint $\sum_{m=1}^M \alpha_m = 1$. $\underline{\tau}^* = 2\mu^* \underline{S} + (\beta^* - 2\mu^*/3)(\nabla \cdot \mathbf{u}) \underline{1}$ is the artificial viscous stress and $\mathbf{q}^* = -\kappa^* \nabla T + \sum_{m=1}^M h_m \mathbf{J}_m^*$ is the artificial heat flux. $\underline{S} = (\nabla \mathbf{u} + \nabla \mathbf{u}^T)/2$ is the strain rate tensor, T is the temperature and μ^* , β^* and κ^* are the artificial shear viscosity, artificial bulk viscosity and artificial thermal conductivity, respectively. The form of artificial properties μ^* , β^* and κ^* used in this paper is the same as that in Ghaisas *et al.* (2016). The second term in the expression for \mathbf{q}^* is the enthalpy diffusion term (Cook 2009) where $h_m = \varepsilon_m + p_m/\rho_m$ is the enthalpy of species m . $(J_m^*)_i = -\rho (D_m^* \partial Y_m / \partial x_i - Y_m \sum_k D_k^* \partial Y_k / \partial x_i)$ is the Fickian diffusive flux for species m in direction x_i and D_m^* is the artificial diffusivity of species m . The form for D_m^* is the same as that used in Subramaniam *et al.* (2017).

To track the deformations in the solid medium, we solve for only the elastic part of the inverse deformation gradient tensor $\underline{\mathbf{g}}^e$, and model the effect of plasticity. The equations governing the evolution of the elastic part of the inverse deformation gradient tensor for material m , $\underline{\mathbf{g}}_m^e$ can be written as in López Ortega *et al.* (2014) and Ndanou *et al.* (2015).

$$\begin{aligned} \frac{\partial (g_m^e)_{ij}}{\partial t} + \frac{\partial u_k (g_m^e)_{ik}}{\partial x_j} &= u_k \left(\frac{\partial (g_m^e)_{ik}}{\partial x_j} - \frac{\partial (g_m^e)_{ij}}{\partial x_k} \right) + \zeta_g \left(\frac{\rho_m}{\rho_{0,m} |\underline{\mathbf{g}}_m|} - 1 \right) (g_m^e)_{ij} \\ &+ \frac{1}{2\mu_m \left(\frac{\rho_m}{\rho_{0,m}} \right) \tau_{0,m}} \left[\frac{R (||\underline{\sigma}'_m||^2 - \frac{2}{3} \sigma_{Y,m}^2)}{\mu_m^2} \right] (g_m^e)_{ik} \sigma'_{kj}. \end{aligned} \quad (2.4)$$

The second term on the right hand side is to ensure consistency with the material density and $\zeta_g = 1/(6\Delta t)$ is a time step dependent constant based on stability considerations.

The last term on the right-hand side of Eq. (2.4) accounts for plasticity effects, where μ_m denotes the shear modulus, $\rho_{0,m}$, density in the undeformed state and $\underline{\sigma}'_m$ is the deviatoric part of $\underline{\sigma}_m$. $\sigma_{Y,m}$ is the yield stress and $1/\tau_{0,m}$, an inverse relaxation time scale of material m . The Ramp function, $R()$, turns off plasticity effects whenever the yield criterion $\|\underline{\sigma}'_m\|^2 = \underline{\sigma}'_m : \underline{\sigma}'_m = \sigma'_{ij,m} \sigma'_{ij,m} < 2\sigma_{Y,m}^2/3$.

In this work, we do not consider effects of plasticity and focus just on problems involving purely elastic deformations and sliding interfaces.

2.1. Constitutive description

An equation of state (EOS) is required to close the above system of equations. We consider a classical hyperelastic form of the EOS, without additional contributions due to capillary/Korteweg effects. The stress is derived from an energy functional based on thermodynamic consistency through the Clausius-Duhem inequality. The internal energy and the resulting Cauchy stress of material m are given by

$$\varepsilon_m = \frac{p_m + \gamma_m p_{\infty,m}}{(\gamma_m - 1) \rho_m} + \frac{\mu_m}{4\rho_{0,m}} \text{tr} \left[\left(\underline{\mathbf{g}}_m^e - \underline{\mathbf{1}} \right)^2 \right] \quad (2.5)$$

$$\underline{\sigma}_m = -p_m \underline{\mathbf{1}} - \mu_m \frac{\rho_m}{\rho_{0,m}} \left(|\underline{\mathbf{G}}_m|^{-2/3} (\underline{\mathbf{G}}_m^2)' - |\underline{\mathbf{G}}_m|^{-1/3} (\underline{\mathbf{G}}_m)' \right), \quad (2.6)$$

where $\underline{\mathbf{G}}_m = (\underline{\mathbf{g}}_m^e)^T \underline{\mathbf{g}}_m^e$ is the elastic Finger tensor, $(\underline{\mathbf{A}})'$ denotes the deviatoric part of the tensor $\underline{\mathbf{A}}$ and $\underline{\mathbf{1}}$ is the identity tensor. Material behavior is described by EOS parameters, γ_m , $p_{\infty,m}$, shear modulus, μ_m , and the undeformed density, $\rho_{0,m}$. This constitutive description is the same as in Subramaniam *et al.* (2017) and Ndanou *et al.* (2015). Note that this constitutive description can be used to model solids ($\mu_m \neq 0$, $p_{\infty,m} \neq 0$), liquids ($\mu_m = 0$, $p_{\infty,m} \neq 0$) and gases ($\mu_m = 0$, $p_{\infty,m} = 0$).

2.2. Numerical solution procedure

We solve the set of Eqs. (2.1)-(2.4) on a fixed Eulerian structured grid using a tenth-order compact finite difference scheme (Lele 1992). A fourth-order five stage Runge-Kutta time integrator (Kennedy *et al.* 2000) is used. The stiff plastic source terms are integrated implicitly, following the method detailed in Favrie & Gavrilyuk (2010). After each stage, the conserved variables are filtered for de-aliasing using an eighth-order compact filter (Lele 1992). Compact finite difference schemes provide spectral-like resolution capabilities but are much more flexible than spectral schemes. The centered schemes used here have no inherent dissipation. Dissipation required for shock and interface capturing is added explicitly through the artificial viscous stress, artificial conductive flux and artificial diffusive flux in Eq. (2.1)-(2.3) as described in Ghaisas *et al.* (2016) and Subramaniam *et al.* (2017).

3. Eulerian continuum sliding treatment

Consider a material interface where the materials on either side are not molecularly bonded. As a consequence, the materials on either side should be allowed to slide past each other. In the absence of friction between the two materials, this means that the traction vector (at the interface) must have no component in the interface parallel direction. Given an interface normal direction $\tilde{\mathbf{v}}_1$, the Cauchy stress $\underline{\sigma}$ should then satisfy the constraint

$$\tilde{\mathbf{v}}^T \underline{\sigma} \tilde{\mathbf{v}}_1 = 0 \quad \forall \tilde{\mathbf{v}} \in \{ \mathbf{x} | \mathbf{x}^T \tilde{\mathbf{v}}_1 = 0 \}. \quad (3.1)$$

In general, the Cauchy stress $\underline{\sigma}$ may not satisfy the constraint in Eq. (3.1). Consider an Eigen decomposition of the Cauchy stress

$$\underline{\sigma} = \underline{V} \underline{\Sigma} \underline{V}^T, \quad (3.2)$$

where $\underline{V} = [\mathbf{v}_1 \mathbf{v}_2 \mathbf{v}_3]$ is an orthogonal matrix and $\underline{\Sigma}$ is a diagonal matrix. \mathbf{v}_1 , \mathbf{v}_2 and \mathbf{v}_3 are the principal directions of $\underline{\sigma}$. These may not be aligned with the interface normal direction as depicted in Figure 1.

The main idea of the algorithm proposed here is to construct a Cauchy stress tensor $\tilde{\underline{\sigma}}$ that does satisfy the constraint Eq. (3.1) and relax the elastic part of the inverse deformation gradient tensor \underline{g}^e to a state consistent with $\tilde{\underline{\sigma}}$. Since the interface traction vector should have no component parallel to the interface, the interface normal $\tilde{\mathbf{v}}_1$ should be a principal direction of $\tilde{\underline{\sigma}}$. We may construct an orthogonal matrix $\tilde{\underline{V}} = [\tilde{\mathbf{v}}_1 \tilde{\mathbf{v}}_2 \tilde{\mathbf{v}}_3]$ (see Figure 1). The constraint Eq (3.1) can then be satisfied by choosing $\tilde{\underline{\sigma}}$ as

$$\tilde{\underline{\sigma}} = \tilde{\underline{V}} \tilde{\underline{\Sigma}} \tilde{\underline{V}}^T \quad (3.3)$$

where $\tilde{\underline{\Sigma}}$ has the following structure

$$\tilde{\underline{\Sigma}} = \begin{bmatrix} \tilde{\Sigma}_{11} & 0 & 0 \\ 0 & \tilde{\Sigma}_{22} & \tilde{\Sigma}_{23} \\ 0 & \tilde{\Sigma}_{23} & \tilde{\Sigma}_{33} \end{bmatrix}. \quad (3.4)$$

Note that, in general $\tilde{\underline{\Sigma}}$ is not a diagonal matrix unlike $\underline{\Sigma}$, since $\tilde{\mathbf{v}}_2$ and $\tilde{\mathbf{v}}_3$ are chosen arbitrarily in the plane orthogonal to $\tilde{\mathbf{v}}_1$. To compute $\tilde{\underline{\Sigma}}$, we can pose consistency conditions between $\underline{\sigma}$ and $\tilde{\underline{\sigma}}$ that the interface normal Cauchy stress is unchanged by the transformation

$$\tilde{\Sigma}_{11} = \tilde{\mathbf{v}}_1^T \underline{\sigma} \tilde{\mathbf{v}}_1 \quad (3.5)$$

and that the stress state in the interface parallel plane is unchanged

$$\tilde{\Sigma}_{ij} = \tilde{\mathbf{v}}_i^T \underline{\sigma} \tilde{\mathbf{v}}_j \quad \forall i, j = 2, 3. \quad (3.6)$$

Given the stress state $\underline{\sigma}$, the transformed stress state $\tilde{\underline{\sigma}}$ is completely defined by Eqs. (3.3)-(3.6). Another interpretation of these consistency constraints is that they define $\tilde{\underline{\sigma}}$ to be the best approximation to $\underline{\sigma}$ by minimizing the error defined by the Frobenius norm $\|\tilde{\underline{\sigma}} - \underline{\sigma}\|_F$ given the constraints in Eq. (3.1) and that $\tilde{\underline{\sigma}}$ is symmetric.

If we split $\underline{\sigma}$ and $\tilde{\underline{\sigma}}$ into an isotropic pressure and a deviatoric stress $\underline{\sigma} = -p\underline{\mathbf{I}} + \underline{\sigma}'$ and $\tilde{\underline{\sigma}} = -\tilde{p}\underline{\mathbf{I}} + \tilde{\underline{\sigma}'}$, for $\tilde{\underline{\sigma}'}$ to satisfy Eq. (3.1), it is sufficient to have $\tilde{p} = p$ and apply the procedure detailed above to compute $\tilde{\underline{\sigma}'}$, given $\underline{\sigma}$.

3.1. Enforcing interface stress conditions

The algorithm described above is only to construct a Cauchy stress $\tilde{\underline{\sigma}}$ that best approximates $\underline{\sigma}$ while still satisfying the sliding interface conditions in Eq. (3.1). Since we use a hyperelastic model to compute the stresses from the elastic inverse deformation gradient tensor \underline{g}^e , we need a relaxation procedure to relax \underline{g}^e to a state that is consistent with $\tilde{\underline{\sigma}}$. In the limit that this relaxation process is instantaneous, we can use an implicit method to relax \underline{g}^e to the desired state as outlined below.

Consider the singular value decomposition of \underline{g}^e

$$\underline{g}^e = \underline{U} \underline{k} \underline{V}^T, \quad (3.7)$$

where \underline{k} is a diagonal matrix with entries k_α , $\alpha = 1, 2, 3$. The eigenvalues of the Finger

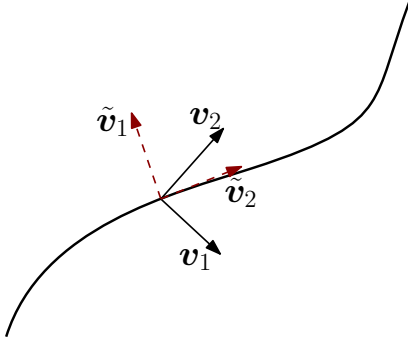


FIGURE 1. Schematic depicting a material interface in two dimensions (solid curved line), the principal stress directions (v_1 and v_2 in solid arrows) and desired principal stress directions (\tilde{v}_1 and \tilde{v}_2 in dashed arrows).

tensor

$$\underline{\mathbf{G}}^e = (\underline{\mathbf{g}}^e)^T \underline{\mathbf{g}}^e = \underline{\mathbf{V}} \underline{\mathbf{K}} \underline{\mathbf{V}}^T \quad (3.8)$$

are given by $\kappa_\alpha = k_\alpha^2$, with $\underline{\mathbf{K}}$ being a diagonal matrix with entries κ_α , $\alpha = 1, 2, 3$.

From Eq. (2.6), we can relate the eigenvalues of $\underline{\sigma}'$ to those of $\underline{\mathbf{G}}^e$ through

$$S_\alpha = -\mu \frac{\rho}{\rho_0} \left[(\kappa_1 \kappa_2 \kappa_3)^{-2/3} \left(\kappa_\alpha^2 - \frac{\kappa_1^2 + \kappa_2^2 + \kappa_3^2}{3} \right) - (\kappa_1 \kappa_2 \kappa_3)^{-1/3} \left(\kappa_\alpha - \frac{\kappa_1 + \kappa_2 + \kappa_3}{3} \right) \right], \quad (3.9)$$

where S_α , $\alpha = 1, 2, 3$ are the eigenvalues of $\underline{\sigma}'$.

Given a deviatoric stress state $\underline{\sigma}'$, we can compute its eigenvalues \tilde{S}_α , and solve for the eigenvalues of the consistent Finger tensor $\tilde{\kappa}_\alpha$ using Eq. (3.9). The eigenvalues of the new consistent $\underline{\mathbf{g}}^e$ are then given by $\tilde{k}_\alpha = \sqrt{\tilde{\kappa}_\alpha} \forall \alpha = 1, 2, 3$. Since the right singular vectors of $\underline{\mathbf{g}}^e$ are the same as the principal directions of the stress, we can reconstruct the consistent $\underline{\mathbf{g}}^e$ up to a rotation factor

$$\underline{\mathbf{g}}^e = \tilde{\mathbf{V}} \tilde{\mathbf{k}} \tilde{\mathbf{V}}^T. \quad (3.10)$$

For isotropic materials, due to objectivity of the stress, any rotation of the $\underline{\mathbf{g}}^e$ tensor does not change the stress state. Previous studies (Barton 2009; López Ortega *et al.* 2014; Subramaniam *et al.* 2017) have used this fact to solve for only the symmetric part of $\underline{\mathbf{g}}^e$ through a polar decomposition $\underline{\mathbf{g}}^e = \underline{\mathbf{R}} \underline{\mathbf{P}}$ where $\underline{\mathbf{R}}$ is a rotation matrix and $\underline{\mathbf{P}} = \sqrt{(\underline{\mathbf{g}}^e)^T \underline{\mathbf{g}}^e}$. The reconstruction of $\underline{\mathbf{g}}^e$ in Eq. (3.10) exactly coincides with the symmetric positive definite factor in its polar decomposition. Since the evolution equation of the symmetric positive definite factor in the polar decomposition of $\underline{\mathbf{g}}^e$ is the same as that of the full $\underline{\mathbf{g}}^e$, there is no loss of information in this reconstruction procedure for isotropic materials.

3.2. Tangential velocity discontinuity in the $\underline{\mathbf{g}}^e$ equation

A sliding interface should support a discontinuous tangential velocity by definition. At a sliding interface, the normal velocity has to be continuous across the interface, but a tangential velocity discontinuity can be supported. Then, the Lagrangian coordinates are

also discontinuous across a sliding interface. In such a scenario, with a diffuse interface treatment, use of Eq. 2.4 across the interface would be inconsistent. Equation (2.4) is for a single continuum field and is not valid across a sliding interface. The spurious effect of a tangential velocity discontinuity at the interface can be remedied by modifying the equation to

$$\begin{aligned} \frac{\partial(g_m^e)_{ij}}{\partial t} + \frac{\partial u_k(g_m^e)_{ik}}{\partial x_j} = & u_k \left[\frac{\partial(g_m^e)_{ik}}{\partial x_j} - \frac{\partial(g_m^e)_{ij}}{\partial x_k} \right] + \zeta_g \left(\frac{\rho_m}{\rho_{0,m} |\mathbf{g}_m|} - 1 \right) (g_m^e)_{ij} \\ & + \frac{1}{2\mu_m \left(\frac{\rho_m}{\rho_{0,m}} \right) \tau_{0,m}} \left[\frac{R(||\boldsymbol{\sigma}'_m||^2 - \frac{2}{3}\sigma_{Y,m}^2)}{\mu_m^2} \right] (g_m^e)_{ik} \sigma'_{kj} + f_{\text{mask}}(g_m^e)_{ik} \left(n_l \frac{\partial u_k^t}{\partial x_l} n_j \right). \end{aligned} \quad (3.11)$$

where \mathbf{n} is the interface normal vector and $\mathbf{u}^t = \mathbf{u} - (\mathbf{n} \cdot \mathbf{u})\mathbf{n}$ is the interface tangential velocity. f_{mask} is a mask function that isolates the sliding term to the interfacial region where it is unity inside and zero outside. The added term on the RHS cancels the effect of the interface normal gradient of the tangential velocity from the equation (in the masked region).

3.3. Interface normal computation and the mask function

For a diffuse interface method, the interface normal may be computed based on the maximal gradients of the volume fraction field $\nabla\alpha_m/|\nabla\alpha_m|$, where α_m is the volume fraction of material m . However, when the interface spans only a few points, the gradient computations are prone to numerical errors and hence the predicted interface normals are not very accurate. A method proposed by Shukla *et al.* (2010) is to use an auxiliary variable ψ given by

$$\psi = \frac{\alpha_m^r}{\alpha_m^r + (1 - \alpha_m)^r}, \quad 0 < r \leq 1. \quad (3.12)$$

For $0 < r \leq 1$, ψ is smoother than the α_m field. If α_m is a hyperbolic tangent profile with a characteristic width δ_α , then ψ has a characteristic width δ_α/r . This auxiliary variable ψ can be used to give a more robust estimate of the interface normal

$$\mathbf{n} = \frac{\nabla\psi}{|\nabla\psi|} = \frac{\nabla\alpha_m}{|\nabla\alpha_m|}. \quad (3.13)$$

In this work, we use $r = 0.5$ for all the examples.

The mask function used in Eq. (3.11) is unity in the interfacial region and zero outside. The specific form of the mask function used in this work is

$$f_{\text{mask}} = 1 - [1 - 4\alpha_m(1 - \alpha_m)]^{n_{\text{mask}}}. \quad (3.14)$$

The exponent n_{mask} can be chosen to make the mask smoother (lower values) or sharper (higher values). Here, we use $n_{\text{mask}} = 40$ to give a sharp mask region.

3.4. Summary of the numerical algorithm

The full algorithm for two materials that share a sliding interface is presented in this section. In one Runge-Kutta time step, the algorithm is as follows.

- (a) Compute the mask function f_{mask} using Eq. (3.14) and the interface normal using Eq. (3.13) at each grid point in the domain;
- (b) Update Eqs.(2.1)-(2.3) and (3.11);

- (c) Set $\tilde{\mathbf{v}}_1$ to be the interface normal \mathbf{n} and construct $\tilde{\mathbf{v}}_2$ and $\tilde{\mathbf{v}}_3$ to be orthogonal to $\tilde{\mathbf{v}}_1$ using Gram-Schmidt orthonormalization or cross-products. Note that these vectors need to have a unit magnitude;
- (d) Compute the deviatoric Cauchy stress $\underline{\sigma}'$ and the corrected interface stress $\tilde{\underline{\sigma}}'$ using Eqs. (3.3)-(3.6); and
- (e) Apply the relaxation procedure detailed in Section 3.1 on the inverse elastic deformation gradient tensor $\underline{\mathbf{g}}^e$.

Typically, interface normals are only accurate close to the interface and hence steps (c-e) in the algorithm can be applied only where $f_{\text{mask}} > \tau_{\text{mask}}$ where τ_{mask} is some threshold value that is chosen to exclude regions far away from the interface. Here, we use $\tau_{\text{mask}} = 0.1$.

4. Results

In this section, we apply the sliding algorithm detailed in Section 3 to one- and two-dimensional problems to test the performance of the algorithm in enforcing the interfacial conditions. All problems are non-dimensionalized based on a density and a pressure scale taken to be the reference density and p_∞ of the first material, $\rho_{0,1}$ and $p_{\infty,1}$ respectively.

4.1. 1D test cases

In this section, we present results from one-dimensional test cases with sliding of two semi-infinite slabs at a material interface. For all the problems considered here, the domain is $x \in [0, L_d]$. Boundary conditions are Dirichlet held at the initial value. The final time of all simulations is such that no waves reach the boundary of the domain. In all cases, the ambient pressure is 0.05, and $\underline{\mathbf{g}}^e$ is set to identity for both materials. EOS parameters are $\rho_{0,1} = \rho_{0,2} = 1$, $p_{\infty,1} = p_{\infty,2} = 1$, $\mu_1 = \mu_2 = 10$ and $\gamma_1 = \gamma_2 = 2.84$ unless otherwise stated, and simulations are performed to a final non-dimensional time of $t = 0.1$.

4.1.1. Sliding of two semi-infinite slabs

The simplest problem involving sliding is of two semi-infinite slabs of material sliding past each other. Here, we simulate this problem with the two materials on either side of the interface being the same. The material interface is initially at $x = 0.5$ with the initial volume fraction profile being a hyperbolic tangent with a characteristic width of $3\Delta_x$, where Δ_x is the grid spacing. The slab on the left initially has a transverse velocity $u_2 = 0.5$ and the slab on the right has an initial transverse velocity $u_2 = -0.5$. The interface normal velocity is 0 everywhere in the domain. Simulations are performed with 400 grid points.

Figure 2(a,b) shows the interface normal and transverse velocities at $t = 0.1$. In the case where the interface does not support sliding, two transverse waves propagate away from the interface that are preceded by normal waves. When the interface is sliding, the correct behavior is observed where the transverse velocity discontinuity stays at the interface without creating any other spurious waves.

4.1.2. Normal shock impinging on a material interface

In this test case, we consider a normal shock impinging on a static material interface. Here, since there is no interface tangential velocity or stress, the solution obtained with and without a sliding interface should be identical. The material interface is initially at $x = 0.65$, with the initial volume fraction profile being a hyperbolic tangent with a characteristic width of $3\Delta_x$, where Δ_x is the grid spacing. Left and right propagating

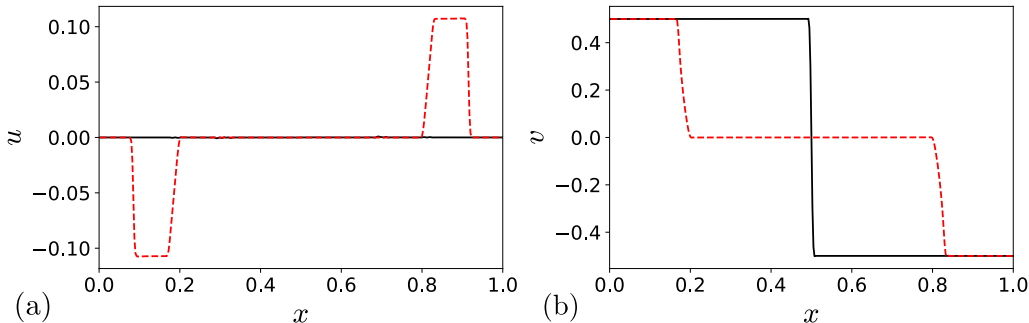


FIGURE 2. Sliding at a material interface between two slabs of the same material at $t = 0.1$. (a) Normal velocity profiles, (b) transverse velocity profiles. Dashed lines: without sliding treatment; solid lines: with sliding treatment.

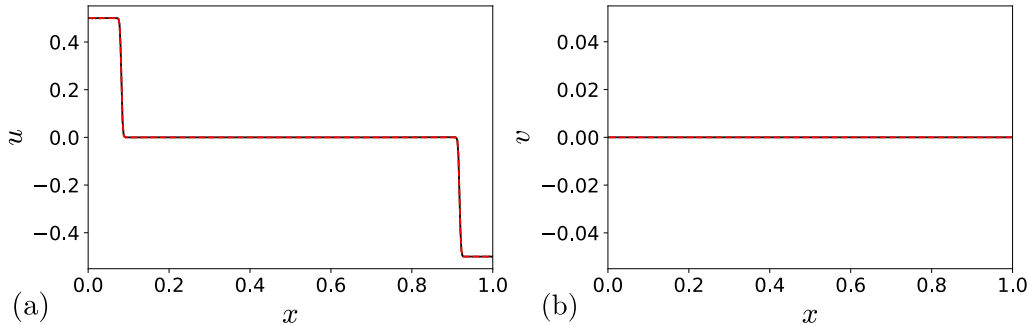


FIGURE 3. Normal wave impinging on a sliding interface between two slabs of the same material at $t = 0.1$. (a) Normal velocity profiles, (b) transverse velocity profiles. Dashed lines: without sliding treatment; solid lines: with sliding treatment.

normal shock waves are set up at $x = 0.5$ with an initial normal velocity $u_1 = 0.5$ for $x < 0.5$ and $u_1 = -0.5$ for $x > 0.5$. The interface tangential velocity is 0 everywhere in the domain. Simulations are performed with 400 grid points.

Figure 3(a,b) shows the normal and transverse velocity profiles at $t = 0.1$. For both cases when the interface does and does not support sliding, we obtain identical results. Since the materials are the same on either side of the interface, the right propagating shock completely passes into the material on the right without any reflections. This result shows that the sliding treatment does not corrupt the behavior of any normal waves passing across the interface.

4.1.3. Transverse shock impinging on a material interface

Here, we consider a transverse shock impinging on a static material interface. The material interface is initially at $x = 0.65$, with the initial volume fraction profile being a hyperbolic tangent with a characteristic width of $3\Delta_x$, where Δ_x is the grid spacing. Left and right propagating transverse waves are set up at $x = 0.5$, with an initial transverse velocity $u_2 = 0.5$ for $x < 0.5$ and $u_2 = -0.5$ for $x > 0.5$. The interface normal velocity is 0 everywhere in the domain. Simulations are performed with 400 grid points.

Figure 4(a,b) shows the velocity profiles at $t = 0.1$. Since the materials on either side of the interface are the same, the right propagating transverse and normal waves pass cleanly across the interface. With sliding, however, the interaction of the transverse wave with the sliding interface creates a reflected transverse wave, and there are no transverse

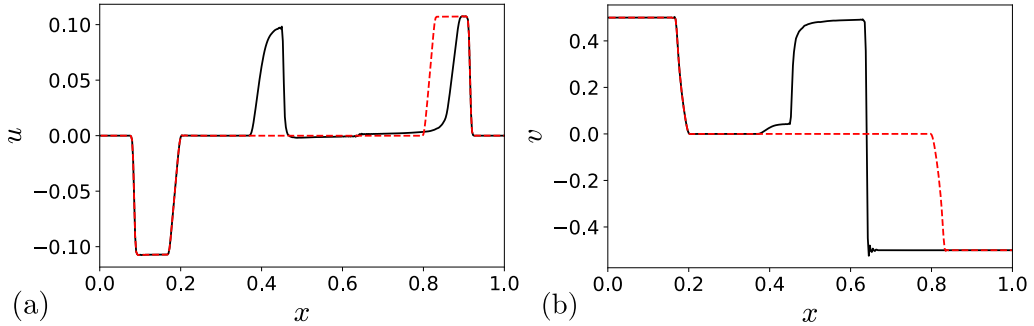


FIGURE 4. Transverse wave impinging on a sliding interface between two slabs of the same material at $t = 0.1$. (a) Normal velocity profiles, (b) transverse velocity profiles. Dashed lines: without sliding treatment; solid lines: with sliding treatment.

waves that propagate into the material on the right. This is the correct behavior since a perfectly sliding interface cannot support any tangential stresses and hence no transverse waves can cross the interface.

In summary, three canonical 1D tests are presented in this section that assess the performance of the sliding treatment, and the correct behavior is obtained for both normal and transverse waves interacting with the sliding interface.

4.2. 2D test cases

4.2.1. Solid body rotation of a cylinder

The first 2D test case is an extension of the problem presented in Section 4.1.1. We consider a rotating cylinder of material 1 embedded in static material 2. The 2D domain is $[-0.5, 0.5] \times [-0.5, 0.5]$. The material interface is at a radius of $r = 0.35$. The initial radial velocity is zero everywhere, and tangential velocity at a radius r is given by $r\omega$, where $\omega = 0.5$ is the angular velocity. The ambient pressure is 0.05, and \mathbf{g}^e is set to identity for both materials. EOS parameters are $p_{\infty,1} = 1$, $p_{\infty,2} = 1$, $\rho_{0,1} = 1$, $\rho_{0,2} = 2$, $\mu_1 = 10$, $\mu_2 = 20$ and $\gamma_1 = \gamma_2 = 2.84$. Simulations are performed on a 128×128 Cartesian grid with a final non-dimensional time of $t = 1$.

In the 1D tests, the interface normal can only be along the x direction, but in this 2D case, the interface normal computation is not trivial and dynamically affects the solution through the sliding treatment. Figure 5 shows the initial and final tangential velocity profile and velocity vectors. Since the interface allows for sliding, the interface tangential velocity discontinuity stays at the interface and no spurious transverse waves are created.

4.2.2. Cylindrical transverse shock impinging on a cylindrical interface

The next 2D test case is similar to the one above, but where the initial tangential velocity discontinuity is not collocated with the material interface. We consider a cylinder of material 1 embedded in material 2. The 2D domain is $[-0.5, 0.5] \times [-0.5, 0.5]$. The material interface is at a radius of $r = 0.35$. The initial radial velocity is zero everywhere and tangential velocity at a radius $r < 0.25$ is given by $r\omega$ where $\omega = 0.5$ is the angular velocity. For $r > 0.25$, the tangential velocity is zero. The ambient pressure is 0.05, and \mathbf{g}^e is set to identity for both materials. EOS parameters are $p_{\infty,1} = 1$, $p_{\infty,2} = 1$, $\rho_{0,1} = 1$, $\rho_{0,2} = 2$, $\mu_1 = 10$, $\mu_2 = 20$ and $\gamma_1 = \gamma_2 = 2.84$. Simulations are performed on a 128×128 Cartesian grid with a final non-dimensional time of $t = 0.1$.

Figure 6 shows the tangential velocity profile and velocity vectors at the initial condi-

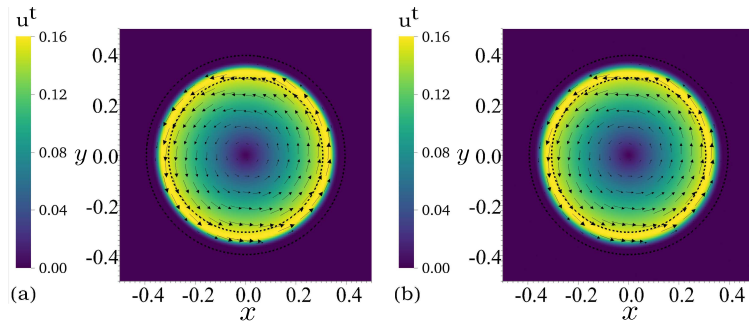


FIGURE 5. Sliding of a circular cylinder embedded in a slab of a different material. Colors: magnitude of the tangential velocity, vectors: velocity vectors and the dashed black lines: $f_{\text{mask}} = 0.5$ contours.

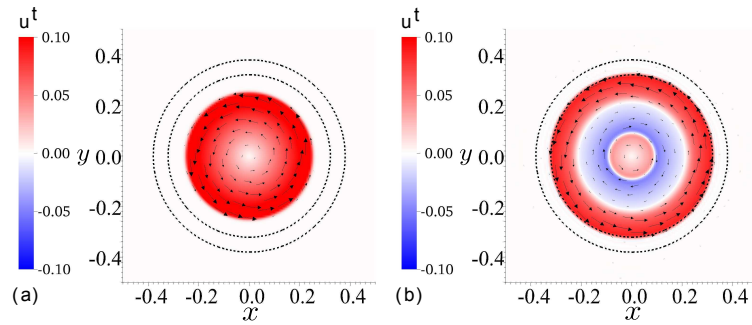


FIGURE 6. Cylindrical transverse shock impinging on a cylindrical interface. Colors: magnitude of the tangential velocity, vectors: velocity vectors and the dashed black lines: $f_{\text{mask}} = 0.5$ contours.

tion and at $t = 0.05$. The initial velocity profile creates a transverse wave propagating outwards. This transverse wave interacts with the sliding interface and creates a slip at the interface and a reflected transverse wave similar to the results in Section 4.1.3. We see that no spurious transverse waves are propagated across the material interface due to the sliding treatment.

4.3. Richtmyer-Meshkov instability of a sliding interface

In this section, we consider the problem of a shock wave interacting with a perturbed material interface. The rectangular domain is $[-2, 4] \times [0, 1]$. The material interface initially has a mean position $x = 0$ and has an initial perturbation. The initial volume fraction of the material on the left is given by

$$\alpha_1 = \frac{1}{2} \left[1 - (1 - 2\alpha_{\min}) \operatorname{erf} \left(\frac{x - \eta(y)}{\delta_t \Delta_x} \right) \right], \quad (4.1)$$

with $\eta(y) = \eta_0 \sin(4\pi y)$, $\alpha_{\min} = 10^{-6}$ and $\delta_t = 3$. Δ_x is the grid spacing used in the x direction. An initial amplitude of $\eta_0 = 0.2/(4\pi)$ is chosen. A right-moving shock is initialized in material 1 at $x = -1$, with a shock pressure ratio of 25 using the Rankine-Hugoniot relations derived from Eq. (2.1)-(2.3) and Eq.(2.4). Like the material interface, the shock is also numerically smeared over a few grid points. The pressure profile across

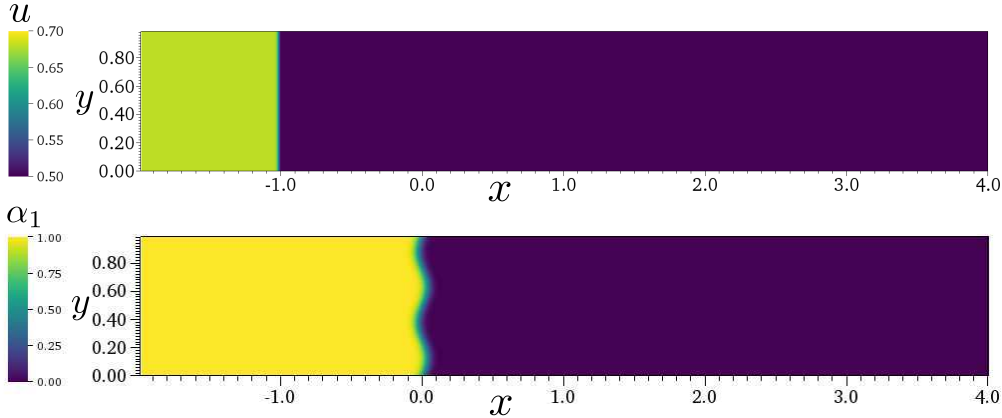


FIGURE 7. Initial normal velocity (top) and volume fraction of material 1 (bottom) in the Richtmyer-Meshkov instability problem.

the shock is given by

$$p = p_1 + \frac{1}{2} (p_2 - p_1) \left[1 - \text{erf} \left(\frac{x - x_s}{\Delta_x} \right) \right], \quad (4.2)$$

where $p_1 = 5 \times 10^{-2}$ is the non-dimensional pre-shock pressure and p_2 is the non-dimensional post-shock pressure. The velocity and density profiles across the shock are also similarly smoothed.

Periodic boundary conditions are used in the y direction. At $x = 4$, a symmetric boundary condition is used to simulate a wall. On the left at $x = -2$, a sponge boundary condition similar to that in Subramaniam *et al.* (2017) is used so that waves reaching this boundary are absorbed and no reflections are transmitted back into the domain.

4.3.1. Same materials on either side of the interface

First, we consider the RM problem with the same material on either side of the interface. The EOS parameters used are the same as in Section 4.1.1. Figure 7 shows the initial u_1 velocity profile visualizing the shock and the volume fraction profile visualizing the interface.

Figure 8 shows the u_1 and u_2 velocity and the z component of vorticity at non-dimensional time $t = 1.5$. When the shock interacts with the perturbed interface, regions of the interface that are not parallel to the shock see a transverse component of velocity and tangential stress. Only the interface normal component of the shock is allowed to pass through while the tangential component is reflected. This creates a transverse wave pattern as is visualized in velocity and vorticity profiles.

Figure 9 compares the u_1 velocity profile at $t = 1.5$ for the case without and with sliding. When sliding is not allowed at the interface, the shock passes unperturbed across the interface since both materials are the same. However, with sliding, there are transverse waves that are generated due to slip at the interface.

4.3.2. Copper-aluminum RM with sliding

Here, we consider the same RM problem but with copper and aluminum on either side of the interface (left and right, respectively). The problem is non-dimensionalized based on the reference density and p_∞ of copper. With this non-dimensionalization, the EOS

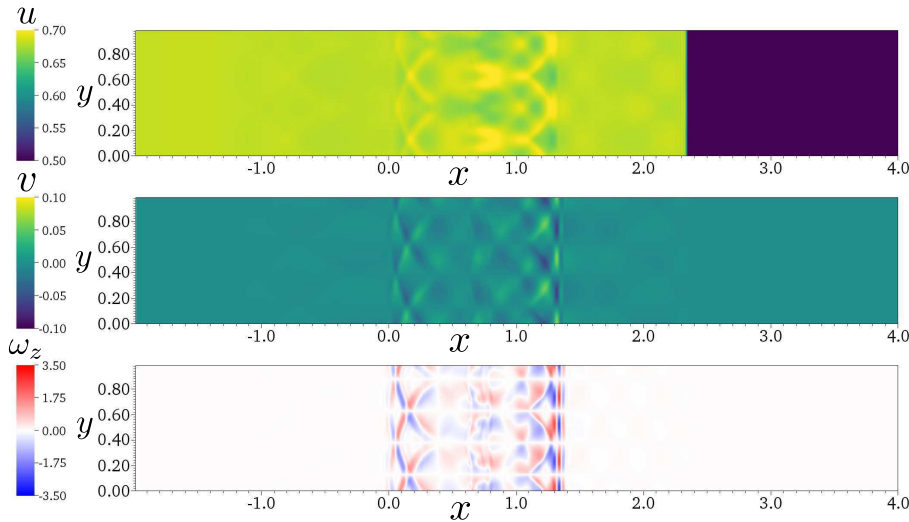


FIGURE 8. u_1 velocity (top), u_2 velocity (middle) and z vorticity (bottom) in the Richtmyer-Meshkov instability problem at $t = 1.5$.

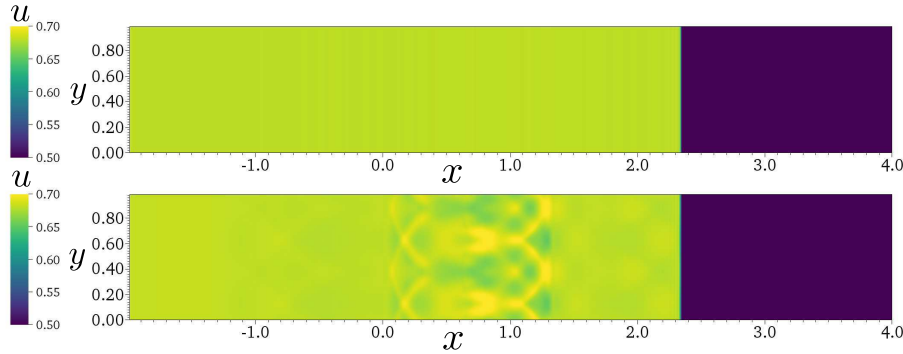


FIGURE 9. u_1 velocity profiles without (top) and with (bottom) the sliding treatment in the Richtmyer-Meshkov instability problem at $t = 1.5$.

parameters are $\rho_{0,1} = 1$, $p_{\infty,1} = 1$, $\mu_1 = 0.2886$, $\gamma_1 = 2$, $\rho_{0,2} = 0.3037$, $p_{\infty,2} = 0.5047$, $\mu_2 = 0.1985$ and $\gamma_2 = 2.088$.

In this problem, since the density ratio across the initial interface is different from unity, interaction of the shock with the interface deposits vorticity on the interface due to baroclinic torque. This vorticity is then transported away from the interface by shear waves. The yield strength of both materials is set to be very large so that plastic deformations do not occur. With sliding, since the transverse component of the shock is reflected and only the normal component is allowed to pass through, stronger oblique waves are generated after the interaction of the shock and the interface. Figures 10 and 11 compare the u_2 velocity profiles between the case with and without sliding at $t = 1.5$ and $t = 3$. In both figures, the case with sliding shows much stronger oblique waves propagating to the right on the aluminum side of the interface. On the copper side of the interface, we see a similar pattern of reflected waves, but also shear waves reflected from the interface.

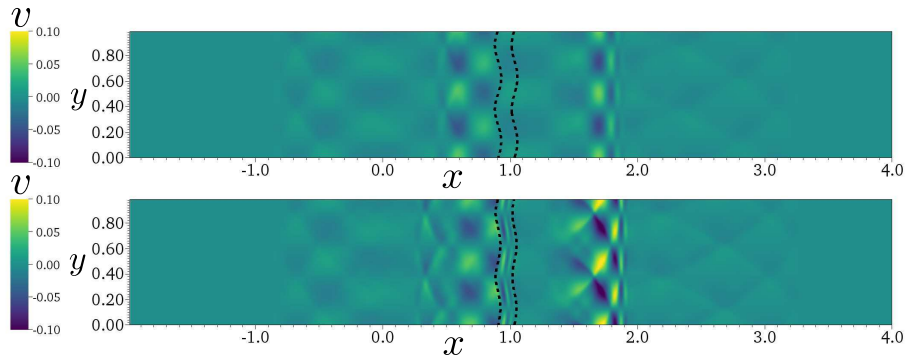


FIGURE 10. u_2 velocity profiles without (top) and with (bottom) the sliding treatment in the copper-aluminum Richtmyer-Meshkov instability problem at $t = 1.5$.

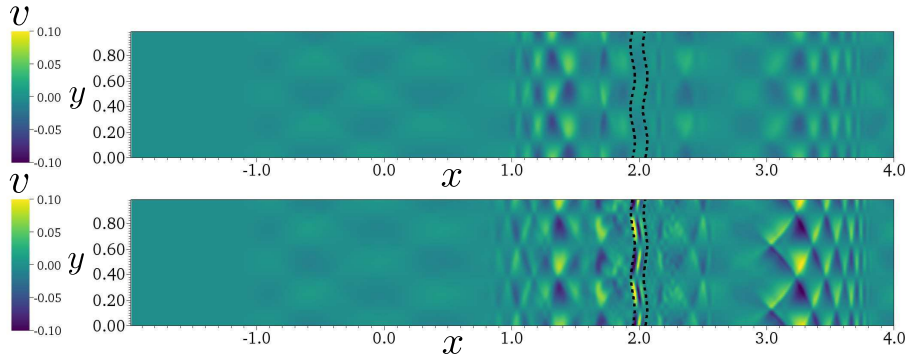


FIGURE 11. u_2 velocity profiles without (top) and with (bottom) the sliding treatment in the copper-aluminum Richtmyer-Meshkov instability problem at $t = 3$.

5. Conclusions

An algorithm for treating perfect sliding in the context of diffuse interface Eulerian simulations of non-linear elasticity has been presented. The algorithm enforces the physical interface boundary conditions based on the principal directions of the Cauchy stress. Consistency conditions are formulated that do not affect the solution when the solution does not require sliding at the interface in order to capture all the relevant interface behavior accurately. This sliding treatment was applied in conjunction with a high-order numerical method for a set of canonical one-dimensional problems. The method was seen to correctly capture the interfacial response to simple sliding, normal waves and shear waves. The method was also applied to two-dimensional problems where the coupling between the interface normal computation and sliding treatment is important and was found to accurately treat the response of a sliding interface. Finally, the Richtmyer-Meshkov instability between copper and aluminum was simulated with an interface that allows for sliding. When compared to the case with a molecularly bonded interface, the transmitted oblique waves were found to be stronger. Sliding at the interface was also seen to create reflected shear waves.

The sliding treatment presented here is general enough to be applied with any diffuse interface numerical model for non-linear elasticity. It can also be applied to solid-fluid interfaces when the fluid is treated as an inviscid fluid. Directions for future work in extending this sliding formulation may include incorporating frictional sliding laws for

solid-solid interfaces and wall models for solid-fluid interfaces that both require allowing for a model specified tangential stress at the interface instead of zero tangential stress for perfect sliding that is used in this work.

Acknowledgments

This work was performed under the auspices of the U.S. Department of Energy by Lawrence Livermore National Laboratory under Contract #DE-AC52-07NA27344. We also thank Dr. Evan Gawlik at UCSD for pointing out the alternate best approximation interpretation of the consistency conditions used to compute $\tilde{\sigma}$.

REFERENCES

- BARTON, P. T. 2009 *A Novel Multi-Dimensional Eulerian Approach to Computational Solid Dynamics*. Ph.D. Thesis, Cranfield University.
- COOK, A. W. 2009 Enthalpy diffusion in multicomponent flows. *Phys. Fluids* **21**, 055109.
- FAVRIE, N. & GAVRILYUK, S. L. 2010 Dynamics of shock waves in elastic-plastic solids. *ESAIM Proceedings* pp. 1–18.
- FAVRIE, N. & GAVRILYUK, S. L. 2012 Diffuse interface model for compressible fluid - compressible elastic-plastic solid interaction. *J. Comput. Phys.* **231**, 2695–2723.
- GHAISAS, N. S., SUBRAMANIAM, A. & LELE, S. K. 2016 High-order Eulerian Methods for Elastic-Plastic Flow in Solids and Coupling with Fluid Flows. *AIAA Paper #3350*.
- GODUNOV, S. K. & ROMENSKII, E. I. 1972 Nonstationary equations of nonlinear elasticity theory in Eulerian coordinates. *J. Appl. Mech. Tech. Ph+* **13**, 868–884.
- KENNEDY, C. A., CARPENTER, M. H. & LEWIS, R. M. 2000 Low-storage, explicit Runge–Kutta schemes for the compressible Navier–Stokes equations. *Appl. Numer. Math.* **35**, 177–219.
- LELE, S. K. 1992 Compact Finite Difference Schemes with Spectral-like Resolution. *J. Comput. Phys.* **103**, 16–42.
- LÓPEZ ORTEGA, A., LOMBARDINI, M., PULLIN, D. I. & MEIRON, D. I. 2014 Numerical simulation of elastic-plastic solid mechanics using an Eulerian stretch tensor approach and HLLD Riemann solver. *J. Comput. Phys.* **257**, 414–441.
- NDANOU, S., FAVRIE, N. & GAVRILYUK, S. L. 2015 Multi-solid multi-fluid diffuse interface model: Applications to dynamic fracture and fragmentation. *J. Comput. Phys.* **295**, 523–555.
- PLOHR, B. & SHARP, D. 1989 A Conservative Eulerian Formulation of the Equations for Elastic Flow. *Adv. Appl. Math.* **9**, 481–499.
- PLOHR, B. & SHARP, D. 1992 A Conservative Formulation for Plasticity. *Adv. Appl. Math.* **13**, 462–493.
- SHUKLA, R. K., PANTANO, C. & FREUND, J. B. 2010 An interface capturing method for the simulation of multi-phase compressible flows. *J. Comput. Phys.* **229**, 7411–7439.
- SUBRAMANIAM, A., GHAISSAS, N. S. & LELE, S. K. 2017 High-Order Eulerian Simulations of Multi-Material Elastic-Plastic Flow. *J. Fluid. Eng.* (In Press), doi: 10.1115/1.4038399.
- TRANGENSTEIN, J. A. & COLELLA, P. 1991 A Higher-Order Godunov Method for Modelling Finite Deformation in Elastic-Plastic Solids. *Commun. Pur. Appl. Math.* **44**, 41–100.